Interfacial thermal transport in spin caloritronic material systems

Frank Angeles,[1] Qiyang Sun,[1] Victor H. Ortiz,[1,2] Jing Shi,[2] Chen Li,[1] and Richard B. Wilson[1,*]
[1]*Department of Mechanical Engineering and Materials Science and Engineering Program, University of California,Riverside, California 92521, USA*
[2]*Department of Physics and Astronomy Program, University of California, Riverside, California 92521, USA*

(Received 24 March 2021; accepted 23 July 2021; published 11 November 2021)

Interfaces often govern the thermal performance of nanoscale devices and nanostructured materials. As a result, accurate knowledge of thermal interface conductance is necessary to model the temperature response of nanoscale devices or nanostructured materials to heating. Here, we report the thermal boundary conductance between metals and insulators that are commonly used in spin-caloritronic experiments. We use time-domain thermoreflectance to measure the interface conductance between metals such as Au, Pt, Ta, Cu, and Al with garnet and oxide substrates, e.g., NiO, yttrium iron garnet (YIG), thulium iron garnet (TmIG), Cr_2O_3, and sapphire. We find that, at room temperature, the interface conductance in these types of material systems range from 50 to 300 $\mathrm{MW\,m^{-2}\,K^{-1}}$. We also measure the interface conductance between Pt and YIG at temperatures between 80 and 350 K. At room temperature, the interface conductance of Pt/YIG is 170 $\mathrm{MW\,m^{-2}\,K^{-1}}$ and the Kapitza length is ~40 nm. A Kapitza length of 40 nm means that, in the presence of a steady-state heat current, the temperature drop at the Pt/YIG interface is equal to the temperature drop across a 40-nm-thick layer of YIG. At 80 K, the interface conductance of Pt/YIG is 60 $\mathrm{MW\,m^{-2}\,K^{-1}}$, corresponding to a Kapitza length of ~300 nm.

DOI: 10.1103/PhysRevMaterials.5.114403

I. INTRODUCTION

Nanoscale devices and nanostructured materials have introduced challenges around thermal management [1]. Specifically, interfacial thermal transport plays a major role in the thermal performance of nanoscale devices and materials [2,3]. A fundamental understanding of interfacial thermal transport is necessary to model and predict nanoscale heat transfer.

An interface between two materials is resistive to heat currents because of differences in vibrational properties. Thermal transport properties at an interface are characterized by the thermal boundary conductance per unit area G [1–4]. Here, G relates the heat current at an interface to the temperature drop ΔT at the interface $J = G\Delta T$. The inverse of G is the thermal boundary resistance. The thermal boundary conductance scales with the irradiance of phonons hitting the interface. The irradiance is proportional to a materials heat capacity and carrier velocities.

The Kapitza length is a useful tool for evaluating the relative importance of an interface to a heat transfer problem. The Kapitza length is the thickness of bulk material that forms an equivalent thermal resistance to the interface [5]. If the Kapitza length is small in comparison with distances between interfaces, the effect of the interface on thermal transport can be neglected. Typical values for the Kapitza length at interfaces between two crystals vary from ~10 nm for epitaxial perovskite oxide interfaces [3] to >10 μm in metal/diamond interfaces [6]. For thin film material systems, the effect of the interface needs to be included in thermal modeling whenever the film thickness is not much greater than the Kapitza length of the interfaces.

The importance of interfacial transport in nanoscale heat transfer problems has motivated extensive experimental and theoretical research [1–7]. Authors of recent studies have clarified the effects different material and interfacial properties have on G [8]. These effects include bulk and interfacial anharmonicity [9], strength of atomic bonds between materials [10], interfacial roughness and structure [11], phonon mean free paths [7], and sample preparation [1]. Experimental data are now available for interface conductance values of many metal/insulator systems [3,5,12,13]. However, experimental data for G between metals and magnetic insulators are sparse.

A lack of experimental data for G between metals and magnetic insulators provides a challenge to the spin caloritronics research community. Spin caloritronics experiments focus on understanding how heat currents and spin currents are coupled in magnetic materials [14]. The geometry of spin caloritronic experiments often involves bulk or thin film magnetic insulators that are coated with a thin metal film [15]. For example, a common geometry for longitudinal spin Seebeck effect measurements involves a thin magnetic insulator, e.g., 100 nm yttrium iron garnet (YIG), sandwiched between a garnet substrate and Pt thin film [16]. A typical thermal conductivity for a garnet crystal is ~ 5 $\mathrm{W\,m^{-1}\,K^{-1}}$ [17,18]. Therefore, the thermal resistance of a thin film in a spin Seebeck experiment at room temperature is ~20 $\mathrm{m^2\,K\,GW^{-1}}$. A typical interface conductance for a metal/insulator system is between 50 and 200 $\mathrm{MW\,m^{-2}\,K^{-1}}$ [1], corresponding to a thermal resistance between 5 and 20 $\mathrm{m^2\,K\,GW^{-1}}$. This implies that, in response to a steady-state heat current, the temperature drop at the

---

[*] fange001@ucr.edu

interface between Pt and the magnetic insulator is comparable with the temperature drop across the entire thin film.

Interpretation of the experimental signals in spin Seebeck effect measurements requires modeling the temperature fields that result from heat currents. Such modeling requires knowledge of interfacial conductance. In the absence of experimental data for G, theoretical models like the acoustic mismatch model are sometimes used to estimate G for the analysis of spin Seebeck experiments [19]. However, the large number of material and interfacial properties that effect G limits the predictive accuracy of simple models [5,6,20,21]. In general, predictions of the acoustic mismatch model and diffuse mismatch model are in poor agreement with experiment [1,21,22]. As a result, a summary of the thermal boundary conductance for a variety of material systems will aid the analysis and interpretation of spin caloritronic experiments by providing them with accurate values.

Here, we report the thermal boundary conductance for a variety of material systems that are common in spin caloritronic experiments. We report G between the metals Al, Cu, Pt, β-phase Ta, and Au with various thin films or single-crystal substrates. The single crystals we study include (111) YIG, (100) gadolinium gallium garnet (GGG), (111) neodymium gallium garnet (NGG), (111) thulium iron garnet (TmIG), (100) nickel oxide (NiO), (0001) chromium oxide (Cr_2O_3), (001) $FePS_3$, (0001) $MnPS_3$, and (0001) sapphire (Al_2O_3). We also report theory calculations for the interface conductance of metal/YIG systems.

At room temperature, we observe interface conductance values for these systems between $25\,\mathrm{MW\,m^{-2}\,K^{-1}}$ and $330\,\mathrm{MW\,m^{-2}\,K^{-1}}$. We observe the smallest conductance values for Al and Ta on the trisulfides $FePS_3$ and $MnPS_3$. We observe the largest conductance between Cu and NiO. The interface conductance of the Cu/insulator and Ta/insulator systems are higher than other metal/insulator interfaces. The conductance of Au/insulator interfaces are lower than in other materials. Since many spin caloritronic experiments are conducted at low temperatures, we also measured G for Pt/YIG vs temperature. We find $60 < G < 170\,\mathrm{MW\,m^{-2}\,K^{-1}}$ for $80 < T < 350\,\mathrm{K}$. At room temperature, the interface conductance of Pt/YIG is $170\,\mathrm{MW\,m^{-2}\,K^{-1}}$, and the Kapitza length is $\sim$40 nm. In experiments where the iron garnet layer is comparable with the Kapitza length, the effect of the interface cannot be neglected in thermal modeling.

II. EXPERIMENTAL METHODS

A. Sample preparation

Metal films were sputter deposited on crystal substrates with an Orion series AJA magnetron sputtering system. Crystal substrates were purchased from MTI. The base pressure of the vacuum chamber before deposition of the metal on all substrates was kept $<\sim 3.5 \times 10^{-7}$ Torr.

Before depositing the metal film, crystal substrates were heated under vacuum to $\sim$600 °C to achieve a clean interface. The substrates were nearly atomically smooth as received with or without annealing (see atomic force microscopy imaging in the Supplemental Material [23]). Rather than altering the surface microstructure, annealing served to eliminate physiosorbed molecules from the surface before metal deposition. The substrates were then allowed to cool for $\sim$4 h. After reaching room temperature, the pressure was raised to 3.5 mTorr by introducing high-purity Ar via a mass flow controller. The power for the metal targets was set according to their diameter. We sputtered Ta, Cu, and Al from 2-inch targets at a power of 200 W. We sputtered Pt and Au from a 1-inch target at a power of 10 W.

The TmIG and Cr_2O_3 crystals were thin films grown via pulsed laser deposition (PLD). The TmIG films were grown on NGG substrates. The NGG substrates were cleaned with acetone/isopropyl alcohol, and then put inside the PLD chamber under high vacuum $\sim 1 \times 10^{-6}$ Torr and baked at 250 °C for at least 5 h. The substrates were then annealed at $\sim$600 °C in a 1.5×10^{-6} Torr oxygen (12% wt. ozone) atmosphere for 30 min; under these conditions, a 248 nm KrF excimer laser pulse was set to strike the TmIG target with a repetition rate of 2 Hz and power (135, 200, and 250 mJ). After the deposition, the samples were annealed *ex situ* at $\sim$800 °C for 300 s under a constant flow of oxygen using rapid thermal annealing. The Cr_2O_3 films were grown on Al_2O_3 single-crystal substrates. The sapphire substrate was cleaned and annealed at 1100 °C for 1 h. Then the substrates were mounted into the PLD chamber and annealed again at 220 °C under high vacuum $\sim 2 \times 10^{-6}$ Torr for 5 h before deposition. The temperature was increased to 600 °C, and an atmosphere of $P = 1.5$ mTorr of ozone/oxygen (12% wt. ozone) was set in the chamber. After 30 min, a 248 nm KrF excimer laser was set to strike a Cr_2O_3 target, using an energy of 156 mJ and a repetition rate of 2 Hz.

To study G between Au, Pt, and Al and various crystals, we sputtered single-layer metal films between 60 and 80 nm thick. With high thermal conductivity and good stability, Au, Pt, and Al are all good transducers for time-domain thermoreflectance (TDTR) experiments [24]. Alternatively, β-phase Ta and Cu are poor transducers for TDTR experiments. Cu is a bad transducer because it does not form a self-limiting oxide. To prevent degradation of the Cu film over time, we capped all 60 nm Cu films with 10 nm of Pt. The 10 nm of Pt prevents oxidation and therefore allows Cu to be used as a transducer. Alternatively, β-phase Ta is a bad transducer because it has a low thermal conductivity of $\sim 4\,\mathrm{W\,m^{-1}\,K^{-1}}$ and has a small thermoreflectance [25]. TDTR measurements lose sensitivity to the thermal conductance of the interface if it is not smaller than the thermal conductance of the metal film. Therefore, we kept the β-phase Ta layer thickness <4 nm and capped it with 60 nm of Pt. The thickness of the Pt layer is much larger than the 9 nm length scale for nonequilibrium between electrons and phonons in Pt [26]. Therefore, nonequilibrium electron-phonon effects, which are sometimes important in metal bilayers, are not important in our experiments [27].

B. TDTR measurements

We used TDTR experiments to measure the thermal boundary conductance. TDTR is a well-established pump/probe technique for measuring thermal properties of thin films and interfaces [28]. TDTR determines thermal properties by measuring the transient evolution of the surface temperature that results from heating by pump pulses. The time evolution of the

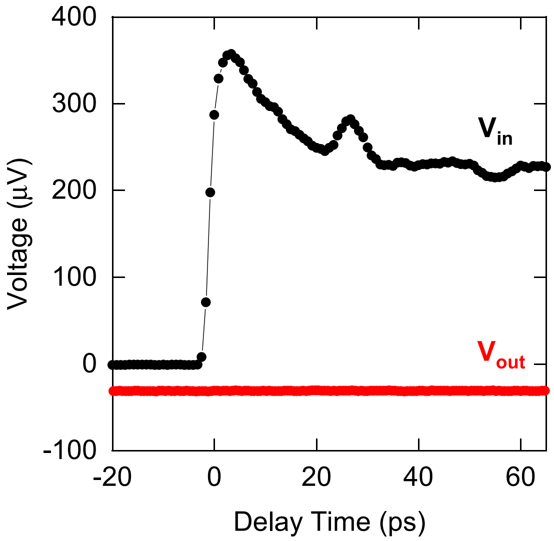

FIG. 1. In-phase and out-of-phase time-domain thermoreflectance (TDTR) data for a 90 nm Al/sapphire sample. Acoustic echoes in the in-phase data at 26.5 and 55 ps provide a measure of the film thickness.

surface temperature is measured with a time-delayed probe pulse. The probe pulse detects temperature-induced changes to the reflectance of the sample. The time required for the metal film to cool after being heated with the pump pulse is determined by the interfacial thermal conductance. The laser spot size in all our experiments was kept constant at $w_0 \approx 6.5\,\mu$m. The pump modulation frequency in our experiments was $f = 10.7$ MHz. The powers of the pump and probe beams were set to keep the steady-state temperature rise for each sample $<\sim 30$ K. The signals of interest in a TDTR experiment are the in-phase and out-of-phase voltages measured by a radio frequency lock in [29]. Figure 1 shows TDTR in-phase voltage V_{in} and out-phase voltage V_{out} data as a function of delay time. The data in Fig. 1 are for an 80 nm Al film on (0001) sapphire substrate. Further details regarding TDTR are available in Refs. [30,31].

We analyzed our experimental data using an analytical solution to the heat diffusion equation in cylindrical coordinates for a multilayer structure [32]. The thermal model takes the thermal properties and thickness of each layer of the multilayer sample as inputs. The model then outputs a prediction for the ratio of the in-phase and out-of-phase voltages $V_{\text{in}}/V_{\text{out}}$. The ratio is large/small for materials with large/small thermal effusivity. The ratio decays faster/slower with time delay for material systems with larger/smaller interface conductance.

The important model inputs are the metal film thickness, the metal film heat capacity, the metal film thermal conductivity, the interface conductance, the heat capacity of the substrate, and the thermal conductivity of the substrate. We set the heat capacity of the transducer and substrates based on literature values [17,33–35].

We measured the thickness of the thin film transducer of our samples using one of two methods: picosecond acoustics or independent TDTR measurement on a dummy sample. For metals where the reflectivity is sensitive to strain, in addition to information about the thermal response, our in-phase signal detects acoustic echoes from the metal/insulator interface [36], see Fig. 1. The longitudinal sound velocity in the metal is taken from literature values [37]. The TDTR data in Fig. 1 for a ∼90-nm-thick Al film on sapphire have picosecond acoustic echoes at delay times of 26.5 and 55 ps. These echo times correspond to the time of flight for an acoustic wave in Al to travel twice and four times the film thickness.

For some metals, e.g., Pt and Au, the picosecond acoustic echoes were not clearly visible in the TDTR signals. Therefore, for the Pt, Au, Cu, and Ta samples, we determined the total thickness of the film with separate TDTR measurements of identical metal films deposited on sapphire (Al_2O_3) substrates. For these samples, the thermal conductivity of sapphire was fixed to the literature value of $35\,\text{W}\,\text{m}^{-1}\,\text{K}^{-1}$ [38]. Then we fitted the TDTR data with our thermal model and treated the metal film as the fit parameter instead of the substrate thermal conductivity. We confirmed the accuracy of this approach with our Al samples. We deduced the same thickness from TDTR measurements on the dummy sample as we did from our picosecond acoustic measurements.

We fixed the thermal conductivity of the metal films using the Wiedemann-Franz law and four-point probe measurements of the electrical resistivity of the metal. For the (10 nm Pt)/(60 nm Cu) and (60 nm Pt)/(4 nm Ta) samples, we assumed the metal/metal thermal interface resistance was negligible based on measurements of similar metal/metal interfaces in Refs. [39,40].

The only parameters for our samples not fixed with literature values or independent experiments are the thermal boundary conductance and the substrate thermal conductivity. We treat these two properties as fit parameters. We adjusted the values of the substrate thermal conductivity and interfacial conductance until model predictions and experimental data agreed. The measured values for the thermal conductivity of the substrates agree with literature [17,18,41]. The thermal conductivity measured for NiO, YIG, NGG, GGG, and TmIG to 19, 6, 5.6, 5.4, and $1.7\,\text{W}\,\text{m}^{-1}\,\text{K}^{-1}$, respectively. The uncertainties in the model inputs such as heat capacity and metal film thickness cause uncertainties in the derived values for substrate thermal conductivity and interfacial conductance. All fit values have the same uncertainty of ∼10%. Example data with model fits are shown in Fig. 2(a).

To verify that our experimental signals were sensitive to the thermal boundary conductance, we calculated sensitivity coefficients of each parameter. The sensitivity coefficient is a representation of how sensitive our experimental signals are to various thermal model parameters λ. The sensitivity coefficient S_λ is defined as the logarithmic derivative of the signal of interest $V_{\text{in}}(t)/V_{\text{out}}(t)$ with respect to the parameter λ. A sensitivity of 0.5 to the thermal conductivity of the substrate Λ_{sub} at a delay time of 100 ps indicates a 10% change in Λ_{sub} causes a 5% change to the ratio $(V_{\text{in}}/V_{\text{out}})_{t=100\,\text{ps}}$. Figure 2(b) shows the sensitivity coefficients for the most important parameters. These include the thermal conductivity of the substrate Λ_{sub}, the thermal boundary conductance G, the thickness of the thin film transducer h_m, the heat capacity C_t of the transducer and substrate C_{sub}. At delay times >2 ns, our measured signals are primarily determined by the interfacial thermal conductance.

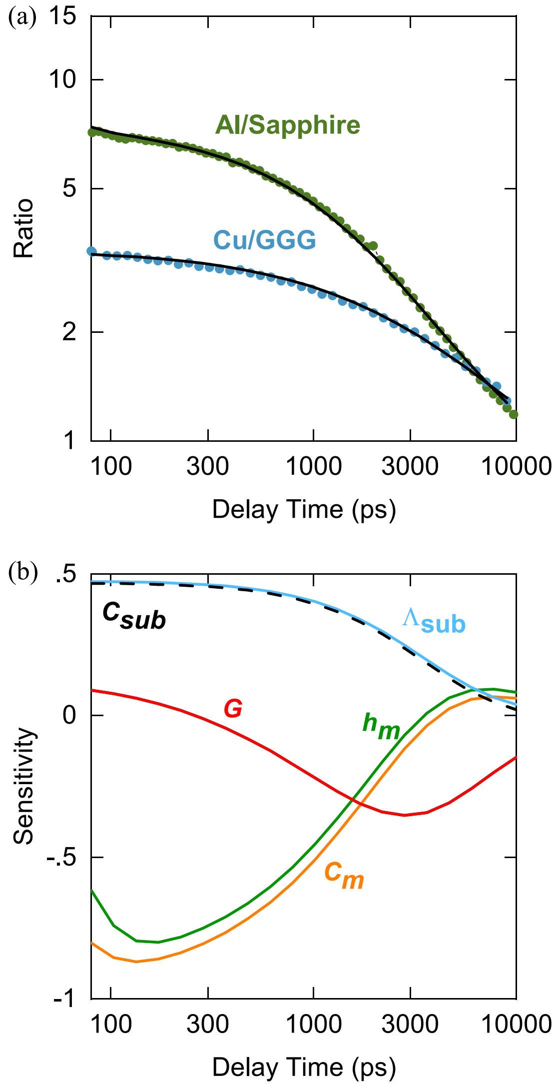

FIG. 2. Results of time-domain thermoreflectance (TDTR) measurements and modeling. (a) Ratio of in-phase and out-phase signals as a function of delay time for Al/sapphire and Cu/gadolinium gallium garnet (GGG) samples. Black lines are fits to the data with our thermal model with $G \approx 180$ and 80 MW m^{-2} K^{-1}, respectively. (b) Sensitivity of our experiment to various parameters. Experimental signals depend on the substrate thermal conductivity Λ_{sub}, the interface conductance G, the metal film thickness h_m, the heat capacity of the transducer C_m, and the heat capacity of the substrate C_{sub}.

In addition to the room temperature measurements described above, we performed TDTR measurements of the Pt/YIG sample at temperatures of $80 < T < 300$ K. For low-temperature measurements, the sample was placed in a vacuum-sealed liquid nitrogen cryostat. The sample was mounted on the cryostat cold finger with silver paste. The cryostat was pumped down to a pressure of $\sim 1 \times 10^{-5}$ Torr and then cooled with liquid nitrogen. The temperature of the cryostat was controlled with a LABVIEW program that interfaced with a LakeShore PID temperature controller (model 335). A cold window on the radiation shield prevented ice formation on the sample during experiments.

III. RESULTS

We report the interfacial conductance results in Fig. 3. We break our conductance measurements into three groups: (a) metal/oxide, (b) metal/iron garnets, and (c) metal/trisulfides. For most insulating materials, we did multiple measurements with different metals. To gauge how changing the metal effects the conductance, Fig. 3 shows the experimental conductance vs the product of the heat capacity and Debye velocity of the metal.

The rationale behind plotting conductance vs $v_D C$ is that interfacial thermal conductance depends on material phonon dispersion. The phonon dispersion relation determines the irradiance of the material, i.e., the number of phonons per unit time that traverse a plane. Materials with large phonon irradiance can form more thermally conductive interfaces then materials with low irradiance [1]. The irradiance is proportional to the product of the phonon number density per unit volume and the phonon speed. Therefore, for simple "Debye-like" materials, $v_D C$ is a good descriptor for irradiance. Prior studies have observed that G of a metal/insulator interface often scales linearly with $v_D C$ of the metal [3].

A. Oxides

The range of conductance values we observe for the metal/oxide samples spans a factor of five, from $G \approx 66$ MW m^{-2} K^{-1} for Au/Al$_2$O$_3$ up to $G \approx 330$ MW m^{-2} K^{-1} for Cu/NiO. We observed the largest values of G for materials with light elements, e.g., Cu on NiO and Al on sapphire.

Experimental values for G are well correlated with $v_D C$ of the metal. We observe average values of 97, 125, 178, and 263 MW m^{-2} K^{-1} for interfaces between oxides and Au, Pt, Ta, and Cu, respectively. These averages scale roughly linearly with $v_D C \approx 3.6$, 5.7, 8.3, and 11.4 GW m^{-2} K^{-1} for Au, Pt, Ta, and Cu, respectively.

Prior studies have emphasized the importance of substrate cleaning and disorder on the interface conductance [20]. We observe small increases in the interfacial conductance value when the surface of the insulating crystal is cleaned before metal film deposition. For example, for Pt/sapphire, we observed an increase in G from 120 MW m^{-2} K^{-1} to $\sim$130 MW m^{-2} K^{-1} when sapphire was at $\sim$600 °C for 30 min before deposition.

B. Iron garnets

The range of interface conductance values we observe for the metal/garnet systems is narrower than for the metal/oxide samples. Conductance values range from 60 MW m^{-2} K^{-1} for Au/GGG to 170 MW m^{-2} K^{-1} for Ta/YIG. Twelve of the 14 samples have conductance values within 40% of 110 MW m^{-2} K^{-1}. For the Au/garnet, Al/garnet, and Pt/Garnet systems, all observed conductance values fall within 30% of one another. For Ta/garnet and Cu/garnet systems, the range of conductance values we observe vary by roughly 60%. Unlike for the metal/oxide samples, we observe no correlation between G and $v_D C$ of the metal.

We report the temperature dependence of the thermal boundary conductance for Pt/YIG in Fig. 4. The conductance decreases from $G \approx 170$ MW m^{-2} K^{-1} at 300 K to

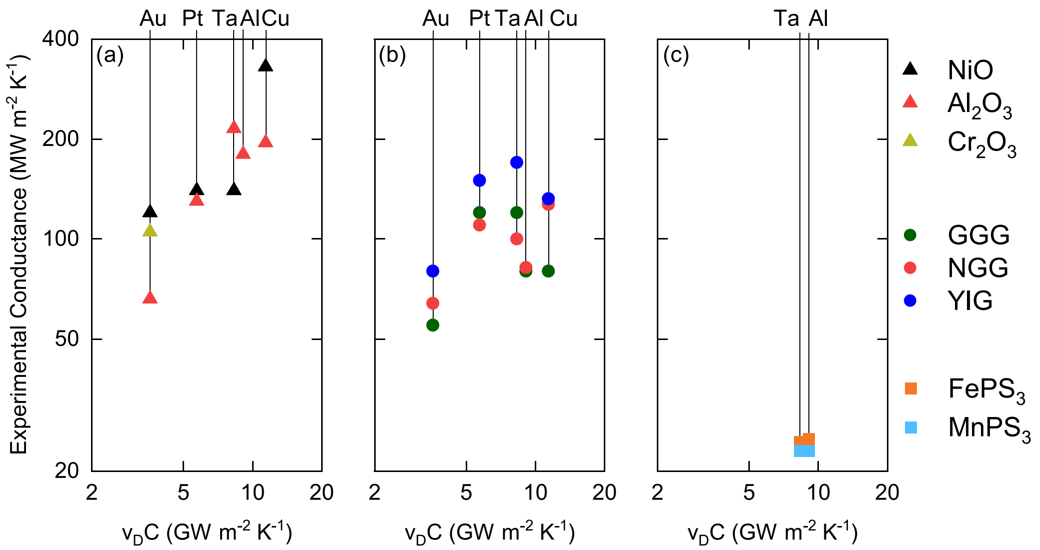

FIG. 3. Results for the interface conductance from time-domain thermoreflectance (TDTR) experiments on (a) metal/oxide, (b) metal/garnet, and (c) metal/trisulfide samples. The x axis is the product of the Debye velocity and heat capacity of the metal v_DC. v_DC has units of conductance per unit area. v_DC is a good descriptor of G for (a) metal/oxides, but a poor descriptor for G in (b) metal/garnet and (c) metal/trisulfide samples.

$\sim$60 MW m^{-2} K^{-1} at 80 K. The temperature dependence of G for Pt/YIG is like the temperature dependence of the heat capacity of YIG. To show that measured values for G track the temperature dependence of the heat capacity of YIG, we include in Fig. 4 the heat capacity of YIG multiplied by a scaling parameter of $\sim$56 m s^{-1}. The temperature-dependent thermal properties of YIG were taken from literature values [42].

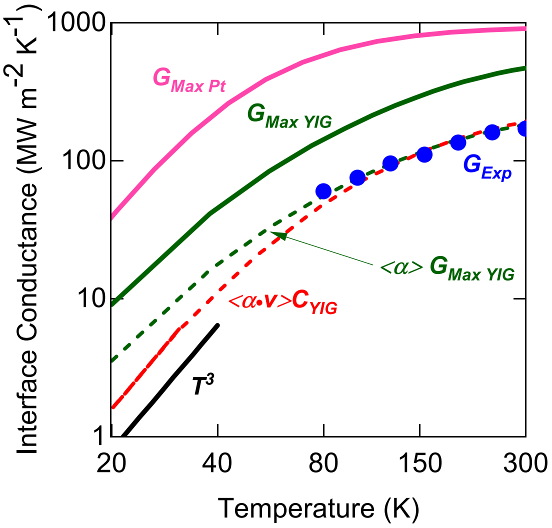

FIG. 4. Temperature dependence of the thermal interface conductance for Pt/yttrium iron garnet (YIG). Experimental values (markers) are compared with the heat capacity of YIG (dashed red line). Theoretical predictions for $G_{\max}$ of YIG and Pt are shown as solid green and pink lines, respectively. G of the Pt/YIG interface is approximately equal to the product of $C_{\mathrm{YIG}}(T)$ and the constant $\langle \alpha v\rangle \approx 56$ m s^{-1}. G is also approximately equal to the product of $G_{\max}$ and $\langle\alpha\rangle \approx 0.4$, see the dashed green line. This means that, for all temperatures we study, the interfacial transmission probability for YIG phonons is $\sim$0.4.

C. Trisulfides

We observe small interface conductances for Ta and Al on the quasi-two-dimensional (2D) materials $MnPS_3$ and $FePS_3$. The conductances we observe for Ta and Al transducers on these crystals are nearly identical, despite Ta and Al having significantly different vibrational properties. The conductance values of $\sim$24 MW m^{-2} K^{-1} are an order of magnitude lower than the conductance values we observe for Ta and Al on garnet and oxide substrates. (The values for Ta on $FePS_3$ and $MnPS_3$ were originally reported in Ref. [43].)

IV. ANALYSIS AND DISCUSSION

A. Model

Interface conductance depends on a variety of factors, including interfacial disorder [9], strength of interfacial bonding [10], and the vibrational properties of the constituent materials [1,3]. Theoretical methods that consider the full array of factors affecting G are complex [44] and beyond the scope of the current experimental study. Instead, we follow Ref. [3] and use a simple model to quantify the effect of the bulk vibrational properties on the interfacial thermal conductance. In our model, we assume the heat current across an interface between material A and B is

$$J = \left[\sum_p \frac{1}{2}\int d\omega\,\alpha(\omega) D_{\omega,p}\frac{\partial n(\omega,T)}{\partial T}\hbar\omega\overline{v_{\omega,z}}\right]\Delta T. \qquad (1)$$

Here, α is the probability of transmission from material A to B, $D_{\omega,p}$ is the density of states of material A at frequency ω and branch p, n is the Bose-Einstein distribution, and $\overline{v_{\omega,z}}$ is the directionally averaged z component of the group velocity of phonons with frequency ω in material A. We define the theoretical maximum conductance $G_{\max}$ as the limit where all phonons in material A that impinge on the interface transmit, i.e., $\alpha = 1$.

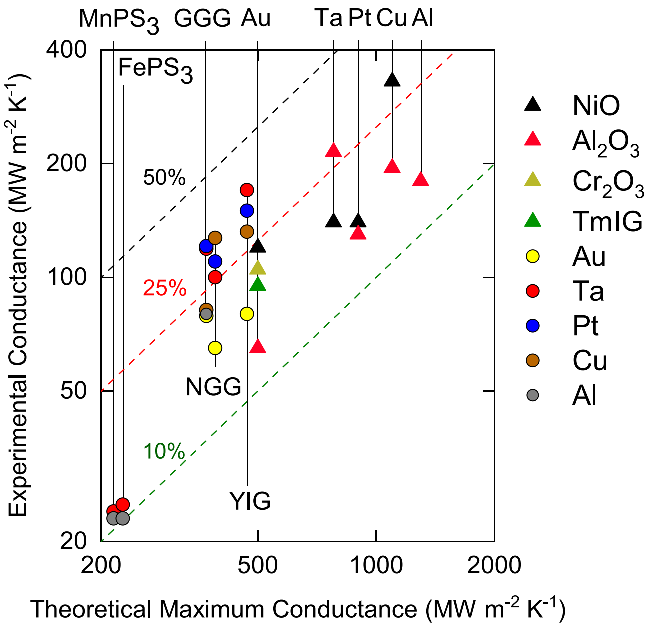

FIG. 5. Comparison of experimental conductance with theoretical values for the maximum possible conductance predicted by Eq. (1). The theoretical maximum conductance corresponds to the limit where the probability of phonon transmission at the interface is unity $\alpha(\omega) = 1$. Green, red, and black dashed lines represent predictions for the conductance when the average transmission probability $\langle\alpha\rangle = 0.1$, 0.25, and 0.5, respectively. Experimental conductance values vary between 0.15 and 0.4 of the theoretical maximum conductance, indicating average interfacial transmission probabilities that vary between 0.15 and 0.4.

While $G_{\max}$ is a property calculated from the phonon dispersion relation of only one material, the maximum conductance $G_{\max}$ at an interface is restricted by the vibrationally softer material. In other words, the conductance at an interface between two materials will be less than $G_{\max}$ of both materials. In Fig. 5, we summarize the experimental values for G vs $G_{\max}$ of the acoustically soft material. The dashed lines in Fig. 5 represent the results of Eq. (1) for the conductance with $\alpha(\omega)$ set to constant values of 0.1, 0.2, and 0.5.

B. Oxides

For the metal/oxide samples, the metal is the acoustically soft material. To evaluate Eq. (1) for the metal/oxide materials, we approximate the dispersion relationship for the metals as an isotropic quadratic function, see Fig. S1 in the Supplemental Material [23]. The $G_{\max}$ values we calculate for the metals are 500 MW m^{-2} K^{-1} for Au, 780 MW m^{-2} K^{-1} for Ta, 900 MW m^{-2} K^{-1} for Pt, 1100 MW m^{-2} K^{-1} for Cu, and 1300 MW m^{-2} K^{-1} for Al.

Overall, we find $G_{\max}$ of the metal to be well correlated with experimental values of G. Most experimental conductance values fall between 0.15 and 0.4 of their respected theoretical maximum value. In other words, the average interfacial phonon transmission coefficient ranges between 0.15 for Au/sapphire up to 0.4 for Cu/NiO.

While $G_{\max}$ is reasonably well correlated with our data, it is not a perfect descriptor. For example, the results for Ta vs Pt metals on the oxides are not well explained by our model. The samples labeled Ta consist of a 4-nm-thick disordered Ta layer with a 60-nm-thick Pt layer on top. Somewhat surprisingly, we find that inserting this thin disordered Ta layer between Pt and the substrate significantly enhances heat transfer between the metal and substrate. The conductance for the Pt/Ta/sapphire sample is roughly twice as large as the Pt/sapphire. The conductance for the Pt/Ta/YIG sample is ~20% larger than for the Pt/YIG sample. Separate TDTR experiments on thick β-Ta films yield a thermal conductivity of only ~5 W m^{-1} K^{-1}. This is ~20× lower than that of Pt. In addition to having a lower thermal conductivity, Ta is vibrationally softer than Pt, as evidenced by a smaller theoretical value for $G_{\max}$. We speculate that the enhanced heat transfer may be due to chemical reactions between the Ta layer and substrate leading to stronger interfacial bonding. Measurements by Monachon *et al.* [45] and Aller *et al.* [46] highlight the important role chemical reactions can play in the thermal boundary conductance between oxide insulators and metals capable of forming oxides.

C. Iron garnets

The Debye velocities of the metals in our material systems range from 1.7 to 4 km s^{-1}. The Debye velocities of the garnets range from 4.1 to 5.1 km s^{-1}. Therefore, a simple comparison of the acoustic velocities suggest Al, Cu, Pt, Ta, and Au are vibrationally softer than garnet insulators. However, the garnet crystals have many atoms per unit cell. A complex unit cell means that most of the vibrations of the crystal are optical phonons with smaller velocities than acoustic phonons. Therefore, the garnets are much vibrationally softer than a simple comparison of Debye velocities suggests.

To account for the low group velocity of optical phonons, we performed density functional theory (DFT) calculations of the phonon dispersion of YIG with the Vienna *Ab initio* Simulation Package (VASP). We provide additional detail on the DFT calculations in the Supplemental Material [23]. We find $G_{\max}$ for YIG of ~400 MW m^{-2} K^{-1}. Due to similarities in crystal structure, we expect GGG and NGG to be vibrationally like YIG. We assume $G_{\max}$ for NGG, GGG, and YIG scale with their Debye velocities. For example, the Debye velocity of GGG is ~20% lower than for YIG, so we estimate $G_{\max}$ for GGG to be ~20% lower than for YIG.

The low $G_{\max}$ prediction of YIG ~400 MW m^{-2} K^{-1} demonstrates the importance of an accurate model for the phonon dispersion relation. Simple models for the phonon dispersion will significantly overestimate the conductance in materials with complex unit cells. For example, the Debye model predicts that $G_{\max}$ is equal to $v_D C/4$, where v_D is the material Debye velocity, and C is the heat capacity per unit volume. The Debye model predicts $G_{\max}$ for YIG of ~3500 MW m^{-2} K^{-1}, a value that is ~10× too large.

Our predictions for $G_{\max}(T)$ are in good agreement with our data, see Fig. 4. At all temperatures we study, G for Pt/YIG is ≈$0.4G_{\max}(T)$ of YIG. Here, G decreases with temperature due to the temperature dependence of the phonon distribution function. At lower temperatures, high-frequency phonons are not thermally excited and do not carry or store heat. For comparison, we also show our predictions for

$G_{\max}(T)$ derived using the phonon dispersion of Pt. Here, $G_{\max}$ for Pt has a markedly different temperature dependence than the experimental data. Therefore, we conclude the conductance of Pt/YIG interfaces is controlled by the bulk vibrational properties of YIG. We can extend this conclusion to the other metal/garnet systems since NGG and GGG have similar vibrational properties and crystal structures to that of YIG.

D. Trisulfides

$FePS_3$ and $MnPS_3$ are quasi-2D-materials. In quasi-2D materials, the flux of vibrational energy in the through-plane direction is small because the anisotropy of these crystals leads to phonon focusing in the in-plane direction [47]. In other words, $MnPS_3$ and $FePS_3$ are vibrationally soft in the through-plane direction, leading to a low conductance. Furthermore, most phonons in $MnPS_3$ and $FePS_3$ are optical modes with small group velocities.

Chen *et al.* [47] describes a model that can account for the effect of anisotropy and phonon focusing on the interface conductance in quasi-2D materials. In the model, the first assumption is that a material anisotropic phonon dispersion can be well approximated by the anisotropic Debye dispersion. The next key assumption is that the first Brillouin zone of an anisotropic material can be adequately approximated by an ellipsoid. The inputs to the model are six sound velocities (three polarizations each of v_a, v_b, and v_c) extracted directly from the phonon dispersion curves [48]. To obtain the sound velocities, a secant method is used, in which case the sound velocity is for a specified branch, and the direction is set to be equal to the slope of the secant that connects the point and the endpoint of that branch at the first Brillouin zone boundary. We use their anisotropic model to predict $G_{\max}$ of 212 MW m^{-2} K^{-1} and 227 MW m^{-2} K^{-1} for $MnPS_3$ and $FePS_3$.

The low values of $G_{\max}$ for $MnPS_3$ and $FePS_3$ explain why the metal/trisulfide interface conductances are significantly lower than the other material systems.

V. CONCLUSIONS

In summary, we report TDTR measurements of the interface conductance between Au, Pt, Ta, Cu, and Al metals with a variety of insulating substrates including NiO, YIG, TmIG, Cr_2O_3, and sapphire. For the metal/garnet and metal/oxide systems, the interface conductance varies by a factor of five, from ~60 MW m^{-2} K^{-1} for Au/NGG to ~300 MW m^{-2} K^{-1} for Cu/NiO. The experimental values for G of metal/oxide interfaces are well correlated with $v_D C$ of the metal. Alternatively, the conductances of metal/garnet and metal/trisulfide interfaces have no correlation with the vibrational properties of the metal. We explain our data with a model that assumes the interface conductance is governed by the vibrational properties of the vibrationally soft material. Garnets are vibrationally soft because the complex unit cell means most vibrations are optical modes with low group velocity. Trisulfides are vibrationally soft due to a large unit cell and phonon focusing effects from anisotropy. We also measured the temperature dependence of G for the Pt/YIG interface. The temperature dependence of G is like the temperature dependence of the heat capacity of YIG, corroborating the assumption of our model that Pt/YIG interfaces are controlled by the bulk vibrational properties of YIG. In general, Our work shows the interface conductance of a spin caloritronic material system is primarily governed by the heat carrying properties of the vibrationally soft material. Finally, our results show that, when modeling interfacial transport, it is important to use accurate models for the phonon dispersion in materials with complex unit cells.

ACKNOWLEDGMENTS

This work was primarily supported by the U.S. Army Research Laboratory and the U.S. Army Research Office under Contract/Grant No. W911NF-18-1-0364. Q.S. and C.L. are supported by the National Science Foundation under Grant No. 1750786. J.S. acknowledges DOE BES Award No. DE-FG02-07ER46351.

---

[1] C. Monachon, L. Weber, and C. Dames, Thermal boundary conductance: a materials science perspective, Annu. Rev. Mater. Res. **46**, 433 (2016).

[2] D. G. Cahill, P. V. Braun, G. Chen, D. R. Clarke, S. Fan, K. E. Goodson, P. Keblinski, W. P. King, G. D. Mahan, A. Majumdar, H. J. Maris, S. R. Phillpot, E. Pop, and L. Shi, Nanoscale thermal transport. II. 2003–2012, Appl. Phys. Rev. **1**, 011305 (2014).

[3] R. B. Wilson, B. A. Apgar, W. P. Hsieh, L. W. Martin, and D. G. Cahill, Thermal conductance of strongly bonded metal-oxide interfaces, Phys. Rev. B **91**, 115414 (2015).

[4] M. D. Losego, L. Moh, K. A. Arpin, D. G. Cahill, and P. V. Braun, Interfacial thermal conductance in spun-cast polymer films and polymer brushes, Appl. Phys. Lett. **97**, 011908 (2010).

[5] M. Blank and L. Weber, Towards a coherent database of thermal boundary conductance at metal/dielectric interfaces, J. Appl. Phys. **125**, 095302 (2019).

[6] R. J. Stoner and H. J. Maris, Kapitza conductance and heat flow between solids at temperatures from 50 to 300 K, Phys. Rev. B **48**, 16373 (1993).

[7] R. B. Wilson, J. P. Feser, G. T. Hohensee, and D. G. Cahill, Two-channel model for nonequilibrium thermal transport in pump-probe experiments, Phys. Rev. B **88**, 144305 (2013).

[8] P. E. Hopkins, Thermal transport across solid interfaces with nanoscale imperfections: Effects of roughness, disorder, dislocations, and bonding on thermal boundary conductance, ISRN Mech. Eng. **2013**, 682586 (2013).

[9] N. Q. Le, C. A. Polanco, R. Rastgarkafshgarkolaei, J. Zhang, A. W. Ghosh, and P. M. Norris, Effects of bulk and interfacial anharmonicity on thermal conductance at solid/solid interfaces, Phys. Rev. B **95**, 245417 (2017).

[10] M. D. Losego, M. E. Grady, N. R. Sottos, D. G. Cahill, and P. V. Braun, Effects of chemical bonding on heat transport across interfaces, Nat. Mater. **11**, 502 (2012).

[11] P. E. Hopkins, L. M. Phinney, J. R. Serrano, and T. E. Beechem, Effects of surface roughness and oxide layer on the thermal boundary conductance at aluminum/silicon interfaces, Phys. Rev. B **82**, 085307 (2010).

[12] R. M. Costescu, M. A. Wall, and D. G. Cahill, Thermal conductance of epitaxial interfaces, Phys. Rev. B **67**, 054302 (2003).

[13] H. K. Lyeo and D. G. Cahill, Thermal conductance of interfaces between highly dissimilar materials, Phys. Rev. B **73**, 144301 (2006).

[14] S. R. Boona, R. C. Myers, and J. P. Heremans, Spin caloritronics, Energy Environ. Sci. **7**, 885 (2014).

[15] I. Oh, J. Park, D. Choe, J. Jo, H. Jeong, M. J. Jin, Y. Jo, J. Suh, B. C. Min, and J. W. Yoo, Solution-processed ferrimagnetic insulator thin film for the microelectronic spin Seebeck energy conversion, ACS Appl. Mater. Interfaces **10**, 28608 (2018).

[16] R. Iguchi, K. I. Uchida, S. Daimon, and E. Saitoh, Concomitant enhancement of the longitudinal spin Seebeck effect and the thermal conductivity in a Pt/YIG/Pt system at low temperatures, Phys. Rev. B **95**, 174401 (2017).

[17] B. S. Wang, H. H. Jiang, Q. L. Zhang, and S. T. Yin, Thermal conductivity of garnet laser crystals, in *High-Power Lasers and Applications IV*, Vol. 6823 (SPIE, Bellingham, 2007), p. 68231P.

[18] Y. Y. Kim, Thermal conductivity of a nanoscale yttrium iron garnet thin-film prepared by the sol-gel process, Nanomaterials **7**, 247 (2017).

[19] M. Schreier, A. Kamra, M. Weiler, J. Xiao, G. E. W. Bauer, R. Gross, and S. T. B. Goennenwein, Magnon, phonon, and electron temperature profiles and the spin Seebeck effect in magnetic insulator/normal metal hybrid structures, Phys. Rev. B **88**, 094410 (2013).

[20] T. Beechem, S. Graham, P. Hopkins, and P. Norris, Role of interface disorder on thermal boundary conductance using a virtual crystal approach, Appl. Phys. Lett. **90**, 054104 (2007).

[21] R. J. Stevens, A. N. Smith, and P. M. Norris, Measurement of thermal boundary conductance of a series of metal-dielectric interfaces by the transient thermoreflectance technique, J. Heat Transfer **127**, 315 (2005).

[22] G. T. Hohensee, R. B. Wilson, and D. G. Cahill, Thermal conductance of metal-diamond interfaces at high pressure, Nat. Commun. **6**, 6578 (2015).

[23] See Supplemental Material at http://link.aps.org/supplemental/10.1103/PhysRevMaterials.5.114403 for for the dispersion curve modeS for platinum and the details for the density functional theory calculations of YIG including Refs. [16,20,49–59].

[24] R. B. Wilson, B. A. Apgar, L. W. Martin, and D. G. Cahill, Thermoreflectance of metal transducers for optical pump-probe studies of thermal properties, Opt. Express **20**, 28829 (2012).

[25] W. P. Hsieh and D. G. Cahill, Ta and Au(Pd) alloy metal film transducers for time-domain thermoreflectance at high pressures, J. Appl. Phys. **109**, 113520 (2011).

[26] H. Jang, J. Kimling, and D. G. Cahill, Nonequilibrium heat transport in Pt and Ru probed by an ultrathin Co thermometer, Phys. Rev. B **101**, 064304 (2020).

[27] R. B. Wilson and S. Coh, Parametric dependence of hot electron relaxation timescales on electron-electron and electron-phonon interaction strengths, Commun. Phys. **3**, 179 (2020).

[28] J. Zhu, X. Wu, D. M. Lattery, W. Zheng, and X. Wang, The ultrafast laser pump-probe technique for thermal characterization of materials with micro/nanostructures, Nanoscale Microscale Thermophys. Eng. **21**, 177 (2017).

[29] S. Miyake, T. Kita, A. Miyake, K. I. Ikeda, and H. Takamatsu, Analysis of thermoreflectance signals and characterization of thermal conductivity of metal thin films, Rev. Sci. Instrum. **80**, 124901 (2009).

[30] M. J. Gomez, K. Liu, J. G. Lee, and R. B. Wilson, High sensitivity pump-probe measurements of magnetic, thermal, and acoustic phenomena with a spectrally tunable oscillator, Rev. Sci. Instrum. **91**, 023905 (2020).

[31] K. Kang, Y. K. Koh, C. Chiritescu, X. Zheng, and D. G. Cahill, Two-tint pump-probe measurements using a femtosecond laser oscillator and sharp-edged optical filters, Rev. Sci. Instrum. **79**, 114901 (2008).

[32] D. G. Cahill, Analysis of heat flow in layered structures for time-domain thermoreflectance, Rev. Sci. Instrum. **75**, 5119 (2004).

[33] B. H. Billings, D. F. Bleil, and D. E. Gray, *American Institute of Physics Handbook* (McGraw-Hill, New York, 1972).

[34] W. F. Giauque and P. F. Meads, The heat capacities and entropies of aluminum and copper from 15 to 300 °k, J. Am. Chem. Soc. **63**, 1897 (1941).

[35] H. Watanabe, Thermal constants for Ni, NiO, MgO, MnO and CoO at low temperatures, Thermochim. Acta **218**, 365 (1993).

[36] G. T. Hohensee, W. P. Hsieh, M. D. Losego, and D. G. Cahill, Interpreting picosecond acoustics in the case of low interface stiffness, Rev. Sci. Instrum. **83**, 114902 (2012).

[37] O. L. Anderson, A simplified method for calculating the Debye temperature from elastic constants, J. Phys. Chem. Solids **24**, 909 (1963).

[38] D. G. Cahill, S.-M. Lee, and T. I. Selinder, Thermal conductivity of κ-Al_2O_3 and α-Al_2O_3 wear-resistant coatings, J. Appl. Phys. **83**, 5783 (2004).

[39] R. B. Wilson and D. G. Cahill, Experimental Validation of the Interfacial Form of the Wiedemann-Franz Law, Phys. Rev. Lett. **108**, 255901 (2012).

[40] B. C. Gundrum, D. G. Cahill, and R. S. Averback, Thermal conductance of metal-metal interfaces, Phys. Rev. B **72**, 245426 (2005).

[41] N. N. Sirota, P. A. Popv, and I. A. Ivanov, The thermal conductivity of monocrystalline gallium garnets doped with rare-earth elements and chromium in the range 6–300 K, Cryst. Res. Technol. **27**, 535 (1992).

[42] M. Guillot, F. Tchéou, A. Marchand, P. Feldmann, and R. Lagnier, Specific heat in erbium and yttrium iron garnet crystals, Z. Phys. B **44**, 53 (1981).

[43] Y. J. Sun, Q. H. Tan, X. L. Liu, Y. F. Gao, and J. Zhang, Probing the magnetic ordering of antiferromagnetic $MnPS_3$ by Raman spectroscopy, J. Phys. Chem. Lett. **10**, 3087 (2019).

[44] S. Sadasivam, N. Ye, J. P. Feser, J. Charles, K. Miao,T. Kubis, and T. S. Fisher, Thermal transport across metal silicide-silicon interfaces: first-principles calculations and Green's function transport simulations, Phys. Rev. B **95**, 085310 (2017).

[45] C. Monachon, G. Schusteritsch, E. Kaxiras, and L. Weber, Qualitative link between work of adhesion and thermal conductance of metal/diamond interfaces, J. Appl. Phys. **115**, 123509 (2014).

[46] H. T. Aller, X. Yu, A. Wise, R. S. Howell, A. J. Gellman, A. J. H. McGaughey, and J. A. Malen, Chemical reactions impede thermal transport across metal/β-Ga_2O_3 interfaces, Nano Lett. **19**, 8533 (2019).

[47] Z. Chen, Z. Wei, Y. Chen, and C. Dames, Anisotropic Debye model for the thermal boundary conductance, Phys. Rev. B **87**, 125426 (2013).

[48] A. Hashemi, H. P. Komsa, M. Puska, and A. V. Krasheninnikov, Vibrational properties of metal phosphorus trichalcogenides from first-principles calculations, J. Phys. Chem. C **121**, 27207 (2017).

[49] G. Kresse and J. Furthmüller, Efficiency of *ab-initio* total energy calculations for metals and semiconductors using a plane-wave basis set, Comput. Mater. Sci. **6**, 15 (1996).

[50] G. Kresse and J. Hafner, *Ab initio* molecular dynamics for liquid metals, Phys. Rev. B **47**, 558 (1993).

[51] G. Kresse and J. Furthmüller, Efficient iterative schemes for *ab initio* total-energy calculations using a plane-wave basis set, Phys. Rev. B **54**, 11169 (1996).

[52] G. Kresse and D. Joubert, From ultrasoft pseudopotentials to the projector augmented-wave method, Phys. Rev. B **59**, 1758 (1999).

[53] V. I. Anisimov, J. Zaanen, and O. K. Andersen, Band theory and Mott insulators: Hubbard U instead of Stoner I, Phys. Rev. B **44**, 943 (1991).

[54] S. F. Maehrlein, I. Radu, P. Maldonado, A. Paarmann, M. Gensch, A. M. Kalashnikova, R. V. Pisarev, M. Wolf, P. M. Oppeneer, J. Barker, and T. Kampfrath, Dissecting spin-phonon equilibration in ferrimagnetic insulators by ultrafast lattice excitation, Sci. Adv. **4**, eaar5164 (2018).

[55] L. S. Xie, G. X. Jin, L. He, G. E. W. Bauer, J. Barker, and K. Xia, First-principles study of exchange interactions of yttrium iron garnet, Phys. Rev. B **95**, 014423 (2017).

[56] V. Cherepanov, I. Kolokolov, and V. L'vov, The saga of YIG: spectra, thermodynamics, interaction and relaxation of magnons in a complex magnet, Phys. Rep. **229**, 81 (1993).

[57] O. V. Prokopenko, D. A. Bozhko, V. S. Tyberkevych, A. V. Chumak, V. I. Vasyuchka, A. A. Serga, O. Dzyapko, R. V. Verba, A. V. Talalaevskij, D. V. Slobodianiuk, Y. V. Kobljanskyj, V. A. Moiseienko, S. V. Sholom, and V. Y. Malyshev, Recent trends in microwave magnetism and superconductivity, Ukr. J. Phys. **64**, 888 (2019).

[58] A. Togo and I. Tanaka, First principles phonon calculations in materials science, Scr. Mater. **108**, 1 (2015).

[59] S. R. Boona and J. P. Heremans, Magnon thermal mean free path in yttrium iron garnet, Phys. Rev. B **90**, 064421 (2014).